materials

MDPI

Article

Oxidation of Al-Co Alloys at High Temperatures

Patrik Šulhánek [1], Marián Drienovský [1], Ivona Černičková [1], Libor Ďuriška [1], Ramūnas Skaudžius [2], Žaneta Gerhátová [1] and Marián Palcut [1,*]

[1] Faculty of Materials Science and Technology in Trnava, Slovak University of Technology in Bratislava, J. Bottu 24, 91724 Trnava, Slovakia; patrik.sulhanek@stuba.sk (P.Š.); marian.drienovsky@stuba.sk (M.D.); ivona.cernickova@stuba.sk (I.Č.); libor.duriska@stuba.sk (L.Ď.); zaneta.gerhatova@stuba.sk (Ž.G.)

[2] Faculty of Chemistry and Geosciences, Vilnius University, Naugarduko g. 24, 01513 Vilnius, Lithuania; ramunas.skaudzius@chgf.vu.lt

* Correspondence: marian.palcut@stuba.sk

Received: 20 June 2020; Accepted: 13 July 2020; Published: 15 July 2020

check for updates

Abstract: In this work, the high temperature oxidation behavior of $Al_{71}Co_{29}$ and $Al_{76}Co_{24}$ alloys (concentration in at.%) is presented. The alloys were prepared by controlled arc-melting of Co and Al granules in high purity argon. The as-solidified alloys were found to consist of several different phases, including structurally complex m-$Al_{13}Co_4$ and Z-Al_3Co phases. The high temperature oxidation behavior of the alloys was studied by simultaneous thermal analysis in flowing synthetic air at 773–1173 K. A protective Al_2O_3 scale was formed on the sample surface. A parabolic rate law was observed. The rate constants of the alloys have been found between 1.63×10^{-14} and 8.83×10^{-12} g cm^{-4} s^{-1}. The experimental activation energies of oxidation are 90 and 123 kJ mol^{-1} for the $Al_{71}Co_{29}$ and $Al_{76}Co_{24}$ alloys, respectively. The oxidation mechanism of the Al-Co alloys is discussed and implications towards practical applications of these alloys at high temperatures are provided.

Keywords: Al alloy; Co alloy; complex intermetallic; oxidation kinetics; oxide scale

1. Introduction

Co-based superalloys are promising materials for high temperature structural applications because of their high melting points and favorable mechanical properties [1–3]. Applications of these alloys include gas turbines, aircraft engines, and chemical reactors [4–6]. The Co-based superalloys are often alloyed with chromium to provide oxidation resistance [7,8]. The superalloys alloyed with Cr form a compact chromia scale (Cr_2O_3) on their surface. Nevertheless, at high temperatures and high oxygen partial pressures, the Cr_2O_3 scale is prone to degradation. During long-term oxidation, volatile high-valent oxides of Cr, such as CrO_2 and CrO_3, start to form at the expense of Cr_2O_3. This effect is called "chromia evaporation" and is often pronounced in humid atmospheres [9]. The loss of protective chromia scale leads to a reduced life span of the Co-based superalloys. Several authors have, therefore, investigated the possibility of improving the high temperature oxidation stability of Co superalloys by alloying with Al [10–12]. Al-based alloys form a protective oxide scale composed of alumina (Al_2O_3). Al_2O_3 has a lower growth rate compared to Cr_2O_3 and is non-volatile. Furthermore, Al is a non-transition element. It has a smaller tendency to form complex oxides with transition metals compared to Cr, thereby reducing the risk of scale spallation over time. The formation of alumina scales may be achieved by pack aluminizing the alloy's surface [13–15]. The application of Al-Co coatings could significantly extend the alloy's lifetime [16–22].

Aluminides are aluminum-based intermetallic compounds with transition metals. Cobalt aluminides are interesting for high temperature applications since they possess a combination of high melting points and good corrosion resistance. At ~18–30 at.% Co, different structurally complex

aluminides in the Al-Co binary system have been observed (Figure 1, [23,24]). These include Al_9Co_2 ($P2_1/C$), Al_5Co_2 ($P6_3/mmc$), Z-Al_3Co (P2/m) and family of $Al_{13}Co_4$ phases containing m-$Al_{13}Co_4$ (C2/m), O-$Al_{13}Co_4$ ($Pmn2_1$), O'-$Al_{13}Co_4$ (Pnma), Y_1-$Al_{13}Co_4$ (C2/m) and Y_2-$Al_{13}Co_4$ (Immm) [25–34]. Although the individual cobalt aluminides are brittle [35], the Al-Co precipitates may significantly strengthen the Al alloys [36,37]. The presence of Al_5Co_2 and $Al_{13}Co_4$ intermetallic compounds (IMCs) may also be beneficial in Co-based alloys as they may greatly improve the alloy's wear resistance [38]. Most aluminides form protective alumina scales with large resistance against corrosion [39].

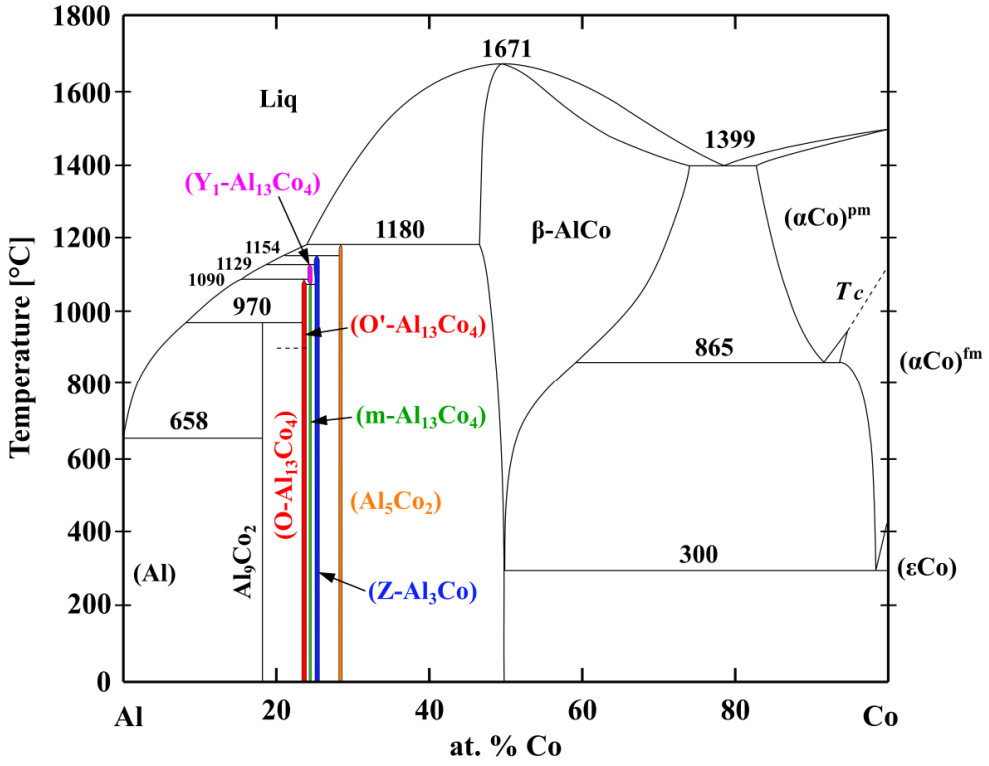

Figure 1. Phase diagram of the Al-Co binary system, redrawn from [23,24].

High temperature corrosion studies of cobalt aluminides are limited. Metal oxidation is a heterogeneous reaction taking place in several elementary steps [40]. In the first step, a gaseous oxygen molecule is transported to the metal surface. Upon approaching the solid phase, the adsorption of oxygen molecules to the metal substrate occurs. Subsequently, the oxygen is dissociated to atoms and later reduced to the O^{2-} anions. In parallel, oxidation of metal atoms takes place at the metal-oxide interface. Recently, M. Wardé et al. studied the adsorption of oxygen on the Al_9Co_2 (001) and $Al_{13}Co_4$ (100) surfaces at high temperatures and reduced oxygen pressures [41]. At the surfaces, only Al–O bonding was observed. Al–O distances were also calculated from first principles [41,42]. The Al–O lengths were shorter in comparison with Co–O distances. The obtained Al–O distances were in agreement with the typical distances of oxygen adsorption on the Al (111) surface, as well as with the Al–O distances in Al_2O_3.

Al-rich Al-Co alloys belong to a relatively new group of complex metallic alloys (CMA, [43,44]). These materials contain structurally complex phases including quasicrystals. The structurally complex phases have non-periodically ordered atomic arrangements [45,46]. Consequently, the properties of CMA are different from those observed in traditional materials [43]. The quasicrystalline surfaces have a good adhesion and low coefficient of friction [47]. Owing to their high hardness and good oxidation resistance, the Al-TM alloys (TM = transition metal) are suitable for high temperature coatings [48–51]. The Al-Co CMAs are also interesting for catalytic and hydrogen generation applications [52–55]. The corrosion studies of Al-Co alloys are limited. Lekatou et al. investigated the

corrosion behavior of an $Al_{82}Co_{18}$ (metal concentrations are given in at.%) alloy in saline solution [56]. Three methods of alloy preparation were investigated: casting, arc-melting and free sintering. The alloy prepared by arc-melting was found to be the most corrosion-resistant. The $Al_{82}Co_{18}$ alloy was composed of (Al), Al_9Co_2 and m-$Al_{13}Co_4$. The complex intermetallic m-$Al_{13}Co_4$ in the alloy was found to have the highest corrosion resistance. Recently, we have investigated the corrosion behavior of as-solidified and near equilibrium Al-Co alloys in various environments [24,57,58]. The alloys were composed of various intermetallic phases. In HCl and NaCl solutions, a pitting corrosion occurred. A higher corrosion resistance of structurally complex Z-Al_3Co phase in Cl-containing electrolytes was observed. The difference in the corrosion behavior could be ascribed to the strong covalent character of metallic bonds in the structurally complex Al-Co phases which prevents aluminum diffusion. The studies also suggest that the existence of an electrical contact between different alloy phases play an important role in the overall alloy's corrosion behavior.

High temperature oxidation studies of Al-Co alloys have been limited to Co-rich alloys only. Zhang et al. investigated the oxidation behavior of Co-5 at.% Al and Co-10 at.% Al alloys at 973 and 1073 K [59,60]. The oxide scales were primarily composed of cobalt oxide and cobalt-aluminum oxide. The oxides grown on these alloys were relatively thick (>10 μm after 24 h). Only a limited amount of Al_2O_3 was found at the inner side of the scales. Irving et al. studied the oxidation behavior of Co-xAl alloys ($0 < x < 32.4$ at.%) at 1073–1273 K [61]. The authors found that 20–25 at.% Al is necessary to form a continuous alumina scale. As such, larger Al concentrations are needed to improve the corrosion resistance of Al-Co alloys.

To our best knowledge, oxidation studies of Al-rich Al-Co alloys have not been reported yet. In the present work, we aim to study the oxidation behavior of Al-rich Al-Co alloys in air at 773–1173 K. Two alloys, $Al_{71}Co_{29}$ and $Al_{76}Co_{24}$ (composition in at.%) were prepared by arc-melting. The composition of the $Al_{71}Co_{29}$ alloy was chosen close to Al_5Co_2 (71.4 at.%). The composition of the $Al_{76}Co_{24}$ alloy was close to $Al_{13}Co_4$ (76.5 at.%). The high temperature oxidation of the alloys was studied with the aim to identify the role of the alloy's chemical composition and microstructure on the overall corrosion behavior.

2. Materials and Methods

The alloys with nominal compositions $Al_{71}Co_{29}$ and $Al_{76}Co_{24}$ (metal concentrations in at.%) were prepared from Co and Al lumps (purity of 99.95%, smart-elements.com) by arc-melting. The melting was conducted in MAM-1 arc melter (Edmund Buehler Ltd., Bodelshausen, Germany) in high purity argon. A piece of Ti (oxygen getter) was melted first to remove residual traces of oxygen in argon. The Co and Al lumps were placed in the center of Cu mold and rapidly melted by striking an arc from tungsten cathode. The homogeneity of the molten samples was improved by repeated arc-melting. Subsequently, the melts were solidified on a water-cooled Cu mold to form button ingots. The as-solidified alloys were removed from the arc-melter, cut into smaller specimens by diamond blade, and prepared for oxidation experiments. The samples were ground with grade 1200 abrasive paper and polished with diamond suspensions down to 1 μm surface roughness.

The oxidation behavior of the polished alloys was studied in flowing synthetic air (20 vol. % O_2 and 80% vol. % N_2). The air flow rate was 20 mL/min. Isothermal oxidation experiments were performed at 773, 973 and 1173 K. The polished samples were placed in an alumina crucible and heated from room temperature to peak temperature by heating rate 20 K/min. The oxidation time was 30 h. The mass gain of the samples was recorded continuously in a chamber of NETZCH STA 409 CD thermogravimeter (NETZSCH-Gerätebau GmbH, Selb, Germany). After oxidation, the samples were cooled down, mounted in epoxy resin, and cut perpendicularly to the reaction interface. The cross-sections of the specimens were prepared by wet grinding and polishing and subjected to microscopy observation.

The microstructure and chemical composition of the alloys was studied by scanning electron microscopy. During experiments, a JEOL JSM-7600F microscope (JEOL Ltd., Tokyo, Japan), equipped with an energy-dispersive x-ray spectrometer X-max (EDS), was used. The EDS was operated by

INCA software (Oxford Instruments Nanoanalysis, Bucks, UK). Regimes of secondary electrons (SE) and backscatter electrons (BSE) were used during imaging. The accelerating voltage of the electron beam was 20 kV and working distance was 15 mm. Furthermore, a Panalytical Empyrean PIXCel 3D diffractometer was used for the phase analysis (Malvern Panalytical Ltd., Malvern, UK). The diffractometer was working with Bragg–Brentano geometry and used $CoK_{\alpha 1}$ radiation. The X-ray beam was generated at 40 kV and 50 mA.

3. Results and Discussion

3.1. Alloy Microstructure and Constitution before Oxidation

The $Al_{71}Co_{29}$ and $Al_{76}Co_{24}$ alloys were prepared by arc-melting. The microstructure of the as-solidified $Al_{71}Co_{29}$ alloy is presented in Figure 2. In this alloy, three different microstructure constituents have been found. The image was acquired in backscatter electron mode to provide element resolution. The chemical composition of the constituents, measured by EDS point analysis, is provided in Table 1. The dendritic constituents have a significantly higher Co concentration (44.8 at.%) compared to the remainder of the alloy. The other two constituents have 28.1 and 25.4 at.% Co, respectively. The black areas, found in the microstructure, are pores.

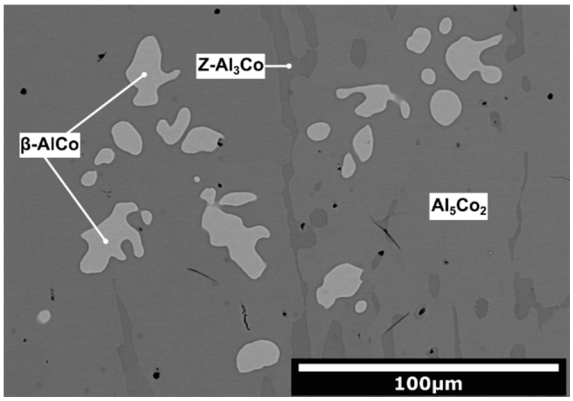

Figure 2. Microstructure of the as-solidified $Al_{71}Co_{29}$ alloy.

Table 1. Chemical compositions of microstructure constituents observed in the as-solidified $Al_{71}Co_{29}$ and $Al_{76}Co_{24}$ alloys.

$Al_{71}Co_{29}$ Alloy				
Microstructure Constituent	**Phase Identified [57]**	**Al [at.%]**	**Co [at.%]**	**Volume Fraction [%]**
Light-grey	β-AlCo	55.2 ± 0.9	44.8 ± 0.9	8
Medium-grey	Al_5Co_2	71.9 ± 0.4	28.1 ± 0.4	86
Dark-grey	Z-Al_3Co	74.6 ± 0.4	25.4 ± 0.4	6
$Al_{76}Co_{24}$ Alloy				
Microstructure Constituent	**Phase Identified [58]**	**Al [at.%]**	**Co [at.%]**	**Volume Fraction [%]**
Light-grey	Z-Al_3Co	74.4 ± 0.1	25.6 ± 0.1	5
Medium-grey	m-$Al_{13}Co_4$	75.2 ± 0.2	24.8 ± 0.2	83
Dark-grey	Al_9Co_2	81.5 ± 0.1	18.5 ± 0.1	12

The microstructure of the as-solidified $Al_{76}Co_{24}$ alloy is presented in Figure 3 in BSE imaging mode. In this alloy, three different microstructure constituents have been found (light grey, medium grey and dark grey). The light grey constituent in the $Al_{76}Co_{24}$ alloy has 74.4 at.% Al and 25.6 at.% Co (Table 1). As such, its chemical composition is comparable to chemical compositions of the dark grey constituent observed in the as-solidified $Al_{71}Co_{29}$ alloy (Figure 2). The medium grey constituent contains 75.2 at.%

Al and 24.8 at.% Co. The dark grey constituent of the as-solidified $Al_{76}Co_{24}$ alloy has 81.5 at.% Al and 18.5 at.% Co. The black areas located within the dark grey constituent are pores (Figure 3).

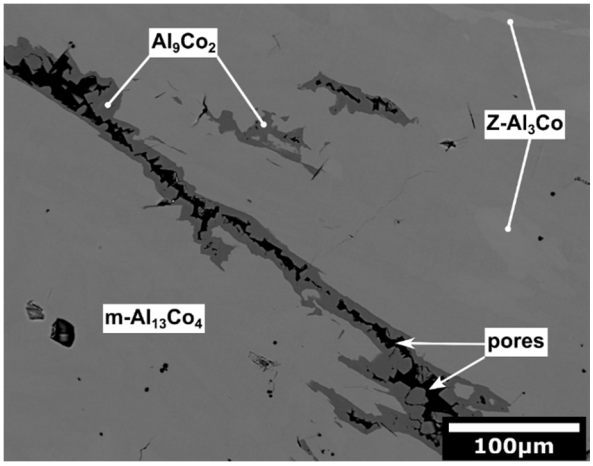

Figure 3. Microstructure of the as-solidified $Al_{76}Co_{24}$ alloy.

A phase assignment of the alloy's microstructure constituents is presented in Table 1. The assignment has been made based on the experimental chemical composition of the constituents obtained by EDS and crystal structure of the phases identified by XRD in our previous work [57,58]. In the studied alloys, altogether five different phases have been identified: β-AlCo, Al_5Co_2, Z-Al_3Co, m-$Al_{13}Co_4$ and Al_9Co_2 (Table 1).

The presence of different phases in the alloys indicates that non-equilibrium processes had been taking place during rapid solidification. The dendritic shape of β-AlCo in the as-solidified $Al_{71}Co_{29}$ alloy suggests that it solidified first, directly from the melt. The dendritic β-AlCo is located inside the Al_5Co_2 phase. Therefore, Al_5Co_2 was probably formed by partial transformation of β. The Al_5Co_2 phase is located next to Z-Al_3Co (Figure 2). As such, Z-Al_3Co was probably formed by peritectic reaction of Al_5Co_2 with the surrounding melt.

The as-solidified $Al_{76}Co_{24}$ alloy was found to consist of Z-Al_3Co, m-$Al_{13}Co_4$ and Al_9Co_2, respectively (Figure 3). The m-$Al_{13}Co_4$ phase is located next to Z-Al_3Co. As such, it was probably formed by peritectic reaction of Z-Al_3Co with the melt. The Z-Al_3Co phase has a lower Al concentration compared to m-$Al_{13}Co_4$ (Table 1). Al_9Co_2, observed in the as-solidified $Al_{76}Co_{24}$ alloy, is located next to m-$Al_{13}Co_4$ (Figure 3). As such, Al_9Co_2 was probably formed by peritectic reaction of m-$Al_{13}Co_4$ with the remaining melt. It was observed to be porous (Figure 3). The pores are usually formed by vacancy migration, with sub-grains and natural surfaces serving as sinks [62,63]. In the present case, the pores were found in the interior of Al_9Co_2. The preferential pore formation indicates that the pores could be a result of rapid transformation of the liquid Al_9Co_2 into solid in the final step of solidification.

3.2. Oxidation Behavior

The oxidation behavior of the as-solidified $Al_{76}Co_{24}$ and $Al_{71}Co_{29}$ alloys was studied in flowing synthetic air at 773, 973 and 1173 K. The microstructure and chemical composition of the oxide scale were investigated by SEM/EDS. The cross-section of the $Al_{71}Co_{29}$ alloy after oxidation at 1173 K is presented in Figure 4. The oxide scale was homogeneous. EDS element maps are included in Figure 4b–d. The scale was found to be composed of aluminum oxide.

The cross-section image of the $Al_{76}Co_{24}$ alloy after oxidation at 1173 K is presented in Figure 5. The thickness of the oxide scale was approximately 1 µm after 30 h of oxidation. The chemical composition of the oxide scale was studied by EDS analysis. Results presented in Figure 5b show that the scale was predominantly composed of Al_2O_3. A small amount of Co (~ 2 at.%) was also detected in the scale, however, this result is attributable to a possible interference of the bulk alloy signal.

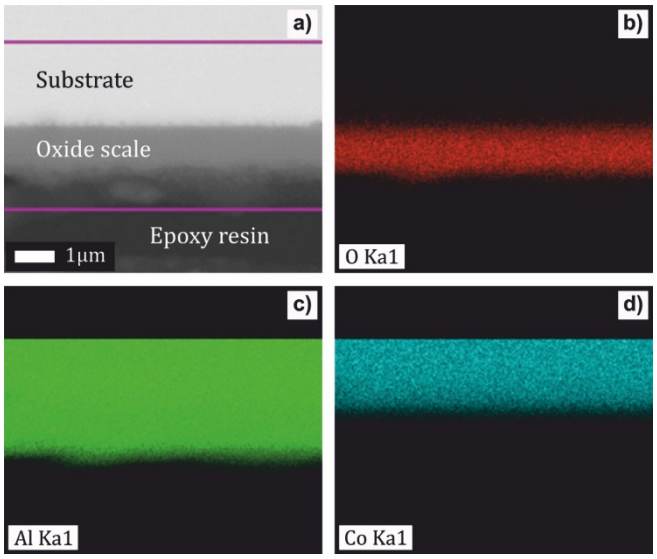

Figure 4. Cross section of the $Al_{71}Co_{29}$ alloy after oxidation at 1173 K for 30 h (**a**) and energy-dispersive x-ray spectrometer X-max (EDS) element maps for O (**b**), Al (**c**) and Co (**d**).

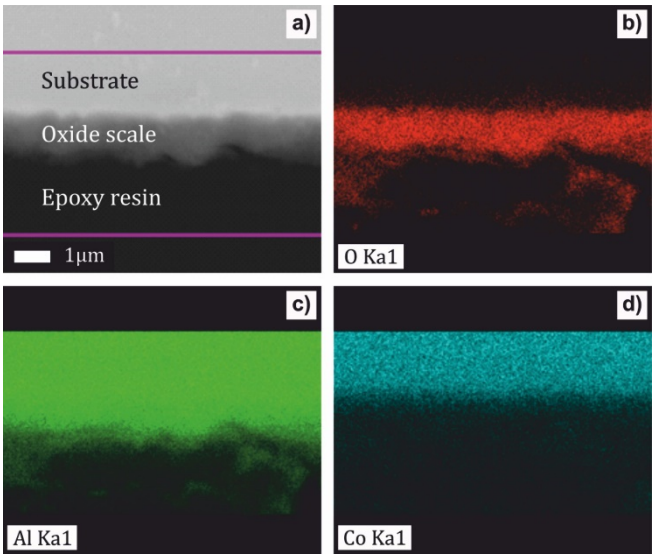

Figure 5. Cross section of the $Al_{76}Co_{24}$ alloy after oxidation at 1173 K for 30 h (**a**) and EDS element maps for O (**b**), Al (**c**) and Co(**d**).

The phase constitution of the oxide scale was studied by room temperature X-ray diffraction. The diffraction patterns of the $Al_{71}Co_{29}$ alloy are presented in Figure 6. In the alloy, peaks corresponding to θ-Al_2O_3 have been identified. θ-Al_2O_3 is a metastable alumina phase [64,65]. θ-Al_2O_3 structures are based on a cubic close packing of oxygen anions. The cubic close packing of oxygen anions of θ-Al_2O_3 is deformed monoclinic. The thermodynamically stable α-Al_2O_3 adopts a corundum structure. θ-Al_2O_3 is a transition phase. It transforms into stable forms of alumina during long term annealing [65]. Metastable θ-Al_2O_3 has been found in oxidized Al-Cu-Fe alloys studied previously [66]. It was formed initially with an orientational relationship to the substrate. At 1173 K, θ-Al_2O_3 was found to slowly transform into α-Al_2O_3 with an increasing oxidation time (70 h, [66]).

At 1173 K, an orientation of θ-Al_2O_3 in (002) crystallographic plane has been found (Figure 6). The same behavior was also observed for the $Al_{76}Co_{24}$ alloy (Figure 6). This observation indicates a preferential crystal growth. The morphology of alumina scale formed on the $Al_{71}Co_{29}$ and $Al_{76}Co_{24}$ alloys after oxidation at 1173 K for 30 h is given in Figure 7. The scale had a blade-like structure.

The platelet-like scale morphology is indicative of rapid outwards growth. Alumina scales grow by counter-diffusion of aluminum and oxygen [67]. The ions, however, diffuse faster in polycrystalline alumina at near-atmospheric oxygen partial pressures. The scale morphology is indicative of rapid diffusion through the scale. A grain boundary diffusion was probably the preferred transport path for the Al^{3+} and O^{2-} ions in the scale.

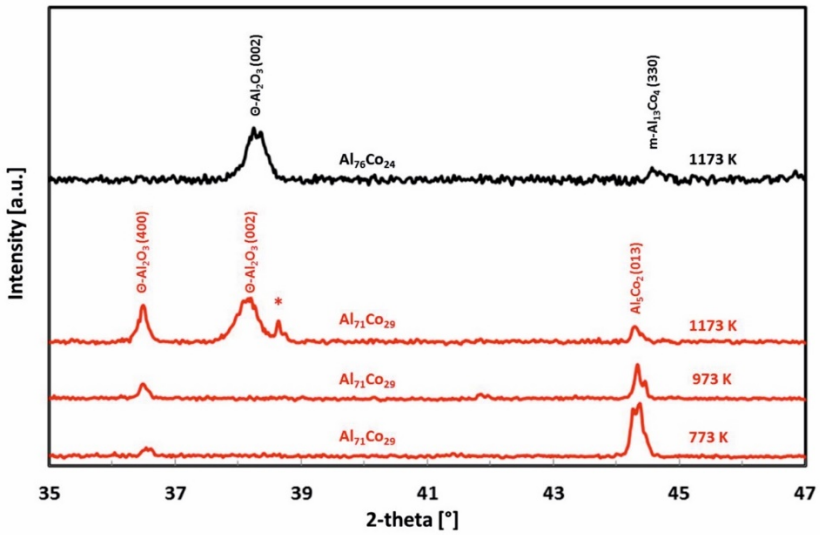

Figure 6. Room temperature XRD patterns of the scales formed on the $Al_{71}Co_{29}$ and $Al_{76}Co_{24}$ alloys. For the discussion of the peak marked with an asterisk (*), please refer to the article text.

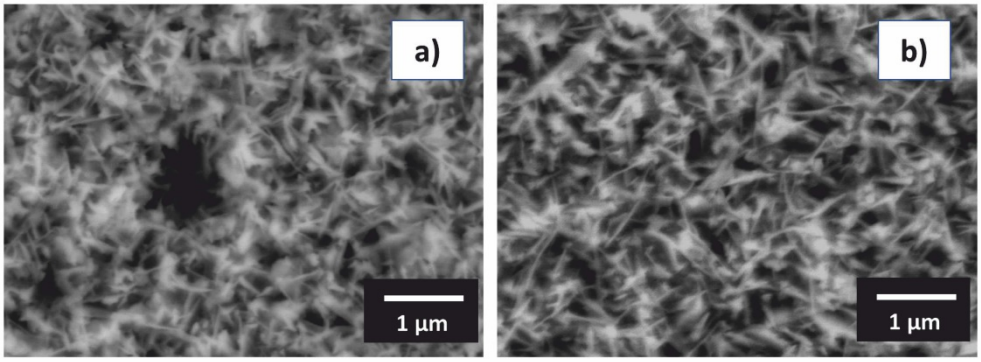

Figure 7. Blade-like morphology of alumina scale formed on the oxidized $Al_{71}Co_{29}$ alloy (**a**) and $Al_{76}Co_{24}$ alloy (**b**) during oxidation at 1173 K.

The un-indexed peak next to θ-Al_2O_3 (002), marked with an asterisk in Figure 6, is an alumina peak. The closest match was found for hexagonal form of Al_2O_3 (reference code 98-017-3713, [68]). Nevertheless, it should also be mentioned that θ-Al_2O_3 has a disordered structure [69–72]. As such, the peak could also be a result of stacking faults (twinning) or other structural defects in θ-Al_2O_3 [73–75]. The precise peak assignment was not possible, owing to the difficulty to unambiguously distinguish the various Al_2O_3 polymorphs by XRD technique alone.

The alumina scale was well adherent to the substrate (Figures 4a and 5a). Nevertheless, locally, a detachment of the scale on the $Al_{71}Co_{29}$ alloy was observed (Figure 8). A scale delamination was found preferentially around β-AlCo dendrites. The situation is shown in Figure 8c. An explanation of the layer spallation could reside in a mechanical stress developed during oxide growth. The stress is formed due to different molar volumes of the oxide and the underlying original metal substrate [76]. The stress generated in the oxide during excessive growth may lead to crack formation in the scale. The pores, cracks and other defects facilitate the access of molecular oxygen to the metal substrate.

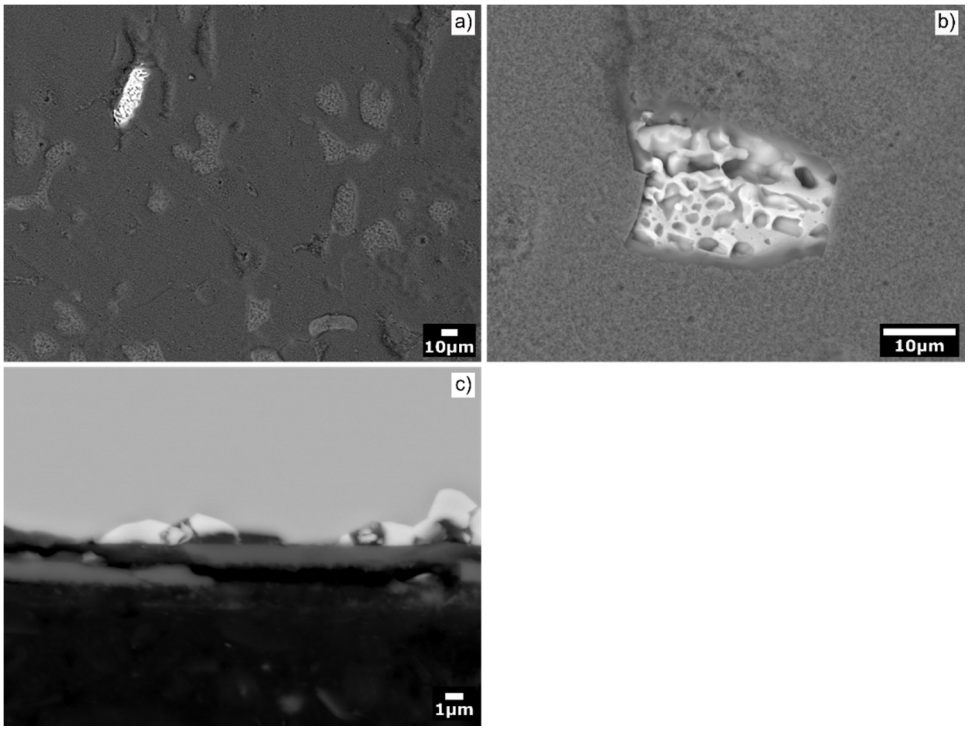

Figure 8. Scale microstructure around β-AlCo dendrites of the $Al_{71}Co_{29}$ alloy: (**a**) an overview; (**b**) a detailed view; (**c**) cross section image of the scale.

Another interesting feature was the porosity of β-AlCo dendrites located beneath the spalled scale of the $Al_{71}Co_{29}$ alloy (Figure 8b). The voids in β-AlCo were not observed before oxidation (Figure 2). The voids were thus formed during reaction, probably because of rapid aluminum outward diffusion from the metal surface. During oxidation, metallic species diffuse out from the alloy bulk to the alloy/oxide interface. The Al atoms, however, leave behind their vacant sites. The vacancies may have coalesced into larger defects, giving rise to the observed macroscopic porosity. The oxide spallation has not been observed on the $Al_{76}Co_{24}$ alloy. The $Al_{76}Co_{24}$ alloy is composed of structurally complex intermetallic phases (Z-Al_3Co, m-$Al_{13}Co_4$ and Al_9Co_2, Figure 3). The surfaces of these phases are typically Al-rich [77]. Aluminum necessary for the scale growth was readily available at the surface of complex intermetallics. As such, the diffusion of Al atoms from these phases was less rapid compared to β-AlCo.

The scale of the $Al_{76}Co_{24}$ alloy did not show any spallation. It was well adherent to the substrate and had a wave-like morphology (Figure 5). The wave-like morphology of the scale could be indicative of epitaxial growth. The XRD pattern showed a preferential orientation of θ-Al_2O_3 grains in (002) crystallographic plane (Figure 6). The θ-Al_2O_3 (400) peak was not observed. The $Al_{76}Co_{24}$ alloy was primarily composed of m-$Al_{13}Co_4$, with small amounts of Z-Al_3Co and Al_9Co_2 (Table 1). A preferred orientation is typical for m-$Al_{13}Co_4$ phase [26,78]. It is therefore likely that the θ-Al_2O_3 phase was formed with an orientation relationship to the m-$Al_{13}Co_4$ phase. This may be reflected in the preferential orientation of the θ-Al_2O_3 grains, as a result of which the intensities of the peaks of this phase change and some may disappear [79,80].

The oxide layer on the $Al_{71}Co_{29}$ alloy, on the other hand, was more uniform (Figure 4). The preferential layer growth is a self-limited process driven by atomic diffusion, and surface energy minimization [81,82]. It requires a certain concentration and certain mobility of Al atoms on the surface. The $Al_{71}Co_{29}$ alloy was primarily composed of Al_5Co_2. The $Al_{76}Co_{24}$ alloy, on the other hand, was mainly composed of m-$Al_{13}Co_4$ (Table 1). The surface of Al_5Co_2 is terminated at specific bulk layers (Al-rich puckered layers) where various fractions of specific sets of Al atoms are missing [83]. The surface of m-$Al_{13}Co_4$ has a higher density of Al atoms when compared to Al_5Co_2. Previous

investigations on $Al_{13}Co_4$ (100) showed that it was terminated by a dense aluminum topmost layer [84]. Therefore, the conditions for the atomic diffusion and subsequent oxide growth on the $Al_{76}Co_{24}$ and $Al_{71}Co_{29}$ alloys were different. The preferential oxide growth was less favored on the $Al_{71}Co_{29}$ alloy.

The mass gain of the samples was recorded by simultaneous thermogravimetry (TGA). Thermogravimetric curves of the $Al_{71}Co_{29}$ and $Al_{76}Co_{24}$ alloys are presented in Figures 9 and 10. The mass gain of the samples was increasing with increasing time. The kinetic curves obeyed a parabolic behavior.

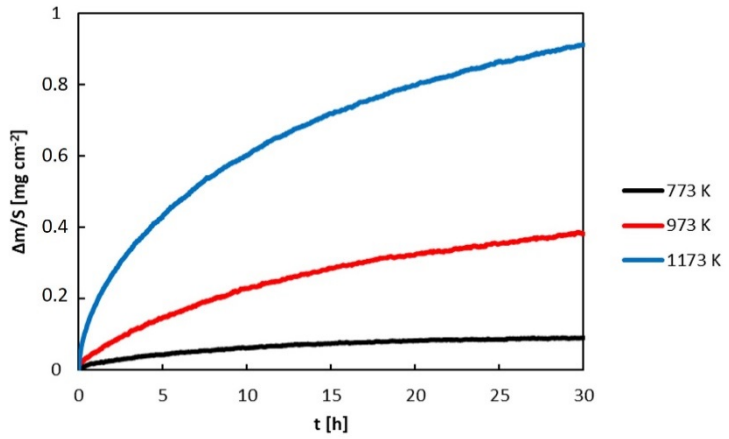

Figure 9. Mass gain of the $Al_{71}Co_{29}$ alloy during isothermal oxidation in flowing synthetic air.

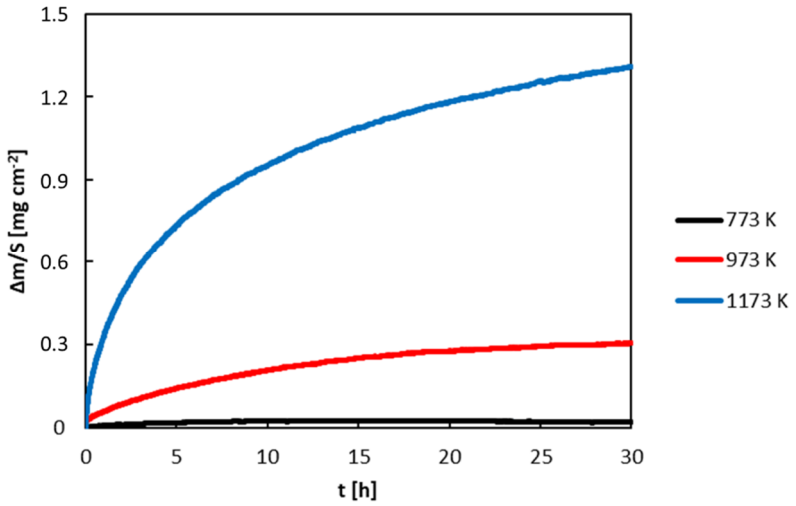

Figure 10. Mass gain of the $Al_{76}Co_{24}$ alloy during isothermal oxidation in flowing synthetic air.

The parabolic oxidation could be described by the following equation

$$\left(\frac{\Delta m}{S}\right)^2 = k_p t + C \quad (1)$$

In this equation, $\frac{\Delta m}{S}$ represents the specific mass gain (mass increase per unit area), k_p is the parabolic constant, t is the annealing time and C is the integration constant. The plot of $\left(\frac{\Delta m}{S}\right)^2$ versus t was linear and the slope of the line represented the parabolic rate constant. The k_p values are collected in Table 2. The rate constants of the alloys are found between 1.6×10^{-14} and 2.5×10^{-11} g^2 cm^{-4} s^{-1}. The obedience of the parabolic behavior shows that the oxidation process of the $Al_{71}Co_{29}$ and $Al_{74}Co_{26}$ alloys was controlled by ionic diffusion in the scale.

Table 2. Parabolic rate constants of the $Al_{71}Co_{29}$ and $Al_{76}Co_{24}$ alloys in air.

k_p [g^2 cm^{-4} s^{-1}]		
$Al_{71}Co_{29}$ Alloy		
773 K	**973 K**	**1173 K**
1.04×10^{-13} (0–15 h) 4.20×10^{-14} (20–30 h)	1.64×10^{-12} (0–15 h) 1.23×10^{-12} (15–30 h)	9.71×10^{-12} (0–15 h) 5.81×10^{-12} (15–30 h)
$Al_{76}Co_{24}$ Alloy		
773 K	**973 K**	**1173 K**
1.63×10^{-14}	1.21×10^{-12} (0–15 h) 5.43×10^{-13} (15–30 h)	2.54×10^{-11} (0–10 h) 8.83×10^{-12} (20–30 h)

Oxidation is a thermally activated process. The parabolic rate constants increase with increasing temperature. The activation energy of oxidation thus could be obtained from the following equation

$$\log k_p = \log A - 0.434\frac{E_A}{RT} \quad (2)$$

In this equation, A is a constant, E_A is the activation energy, R is the molar gas constant (8.3144 J K^{-1} mol^{-1}) and T is the absolute temperature (in K). The plot of rate constants at different temperatures is presented in Figure 11. The rate constants follow the Arrhenius-type behavior. Activation energy has been found from the slope of lines given in Figure 11. The activation energy of the $Al_{71}Co_{29}$ alloy is 90 kJ mol^{-1} and the activation energy of the $Al_{76}Co_{24}$ alloy is 129 kJ mol^{-1}. These activation energies are comparable to activation energies for Al oxidation reported by previous studies [85,86].

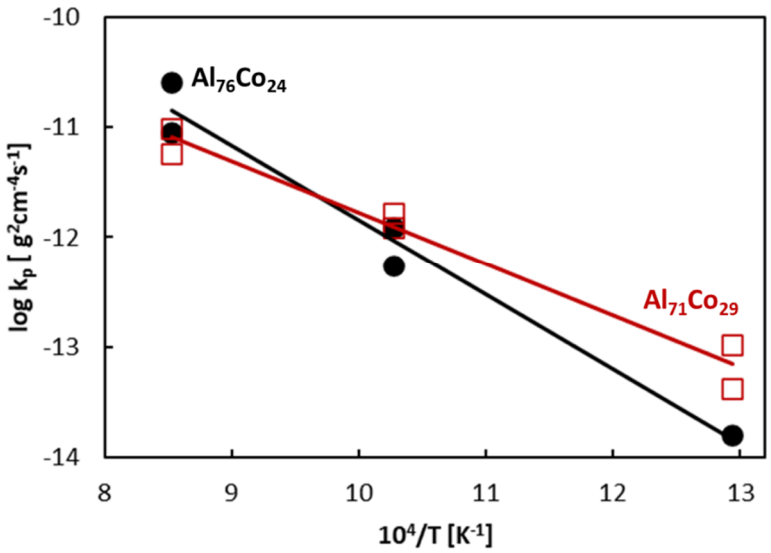

Figure 11. Temperature dependence of parabolic rate constants of the Al-Co alloys.

Results presented above show that a protective scale has been formed on the surface of complex metallic alloys. The rate constants were relatively low, and a thin alumina scale was found on the surface (Figures 4 and 5). Alumina is formed by the following reaction

$$\frac{4}{3}Al + O_2 \rightarrow \frac{2}{3}Al_2O_3 \quad (3)$$

The Gibbs energy (ΔG) of reaction (3) is given in Figure 12. $\Delta G(Al_2O_3)$ is very low which indicates a strong affinity of aluminum towards oxygen. In principle, cobalt oxidation in the Al-Co alloys is also possible. This reaction can be given by the following equation

$$2Co + O_2 \rightarrow 2CoO \quad (4)$$

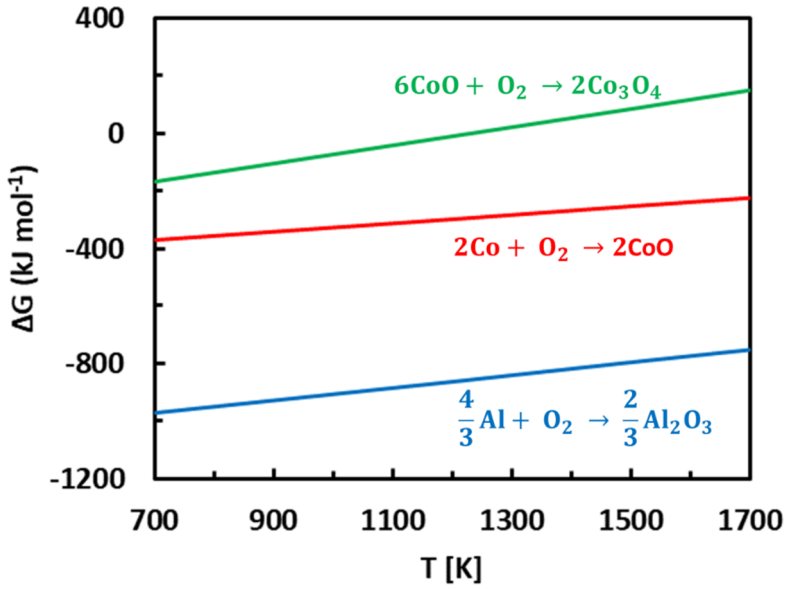

Figure 12. Gibbs free energies of metal oxidation reactions at elevated temperatures, redrawn from [54].

Nevertheless, ΔG reaction (4) is considerably larger compared to Gibbs free energy for aluminum oxidation (Figure 12). A further oxidation of CoO is even more energetically demanding [87,88]. Therefore, CoO tends to decompose in reaction with Al. The reaction can be expressed by the following equation

$$\frac{4}{3}Al + 2CoO \rightarrow \frac{2}{3}Al_2O_3 + Co \quad (5)$$

In this disproportionation reaction, CoO is reduced, and Al oxidized. The Gibbs energy of reaction (5) is negative. Therefore, the selective oxidation of aluminum in the Al-Co alloys is thermodynamically possible.

The oxidation of Co-rich Al-Co alloys was previously studied by Irving et al. [61]. The alloys were studied in the as-cast state. The authors studied several Co-xAl alloys with x = 0–32 at.%. Alloys with small Al concentration (< 10 at.%) formed a single CoO layer. Cobalt oxide layer grew with a considerably higher corrosion rate compared to Al_2O_3. At intermediate Al concentrations (10–20 at.%), the authors found that an inner layer of Al_2O_3 started to form below the outer CoO scale. With increasing aluminum concentration, a continuous Al_2O_3 scale has been developed. The comparison of the present results with those from literature is given in Figure 13. Our data complement the previous results of Irving et al. The continuous Al_2O_3 scale forms a barrier to cobalt diffusion. It hinders the nucleation and growth of cobalt oxides. Irving et al. found that a protective alumina scale can be formed when Al concentration 24 at.% at 1173 K is reached. Comparable minimum Al concentrations required to form the external alumina scale were also found for the Ni-Al and Fe-Al alloys [89].

The comparison of the present results with previously studied complex metallic alloys is provided in Figure 14. Kinetics of oxidation of Al-Cu-Fe and Al-Pd-Mn quasicrystal surfaces was studied in synthetic air [66,90]. High temperature oxidation kinetics of Al-Cr-Fe complex metallic alloys was studied in pure oxygen [91]. Our data are comparable to Al-Cu-Fe and Al-Pd-Mn alloys. The parabolic rate constants of the Al-Cr-Fe complex metallic alloys are lower compared to the remainder of the

alloys. The oxidation resistance of the Al-Fe-TM (TM = Cr, Cu) alloys is related to the chemical composition of the oxide scale. The scale found in Al-Cu-Fe alloys was alumina. The scale formed in Al-Cr-Fe complex metallic alloys, however, was composed of Al_2O_3 and $(Al_{0.9}Cr_{0.1})_2O_3$. The second scale component provided an additional barrier against corrosion. Chromium as a third alloying element may improve the overall oxidation resistance of the alloy. The corrosion resistance of alumina forming alloys alloyed with chromium is higher compared to alloys without Cr. When a sufficient Cr concentration is available, a complete chromia scale can be formed on top of the alumina scale [92,93]. The duplex Al_2O_3/Cr_2O_3 scale has an outstanding corrosion resistance.

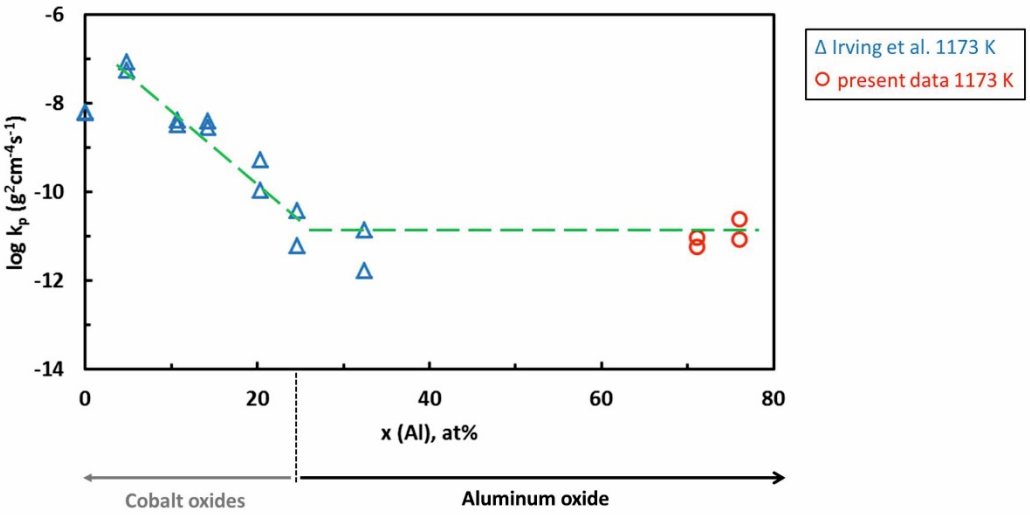

Figure 13. Variation of parabolic rate constants of Al-Co alloys with increasing aluminum atomic fraction.

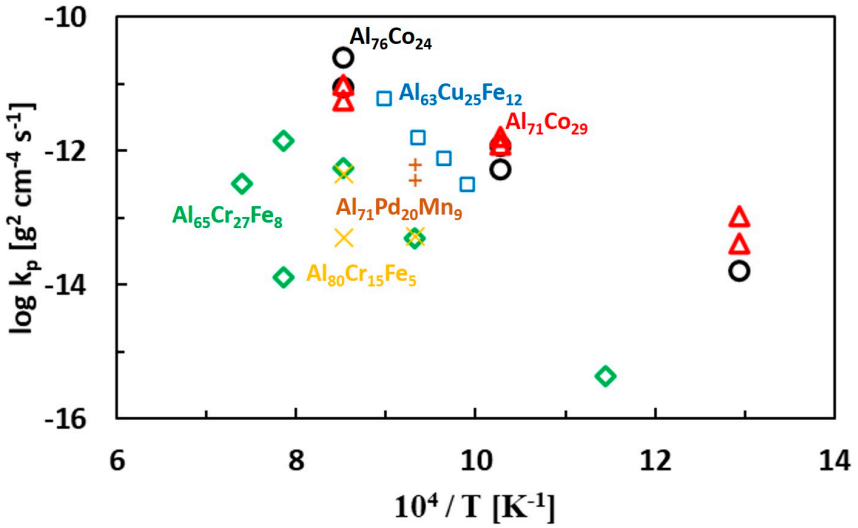

Figure 14. Parabolic rate constants for metal oxidation of Al-TM complex metallic alloys.

Previous authors also studied the microstructure evolution of the oxide scale. In early oxidation stages, γ-Al_2O_3 on the $Al_{63}Cu_{25}Fe_{12}$ alloy was formed with an orientational relationship to the underlying Al-Cu-Fe quasicrystal [66]. γ-Al_2O_3 continued to grow as θ-Al_2O_3 until the oxide layer of several hundred nanometers has been formed. θ-Al_2O_3 was later transformed into the thermodynamically stable α-Al_2O_3. α-Al_2O_3 continued to grow with a nodular morphology. The oxide-nodule formation changed the growth mechanism. A protective layer formation was no longer observed. A massive spallation occurred after few days of oxidation [66]. A spallation of Al_2O_3

scale from the oxidized Al-Cr-Fe surfaces at high temperatures was also observed [91]. The massive oxide spallation has not been observed in the present study. However, the oxide spallation was observed locally on β-AlCo dendrites (Figure 8). It is possible that further stresses in the scale could develop during long term annealing. Therefore, further experiments on the Al-Co complex metallic alloys are required to study the effects of long-term annealing and/or thermal cycling on the oxidation behavior. These studies could shed further light into the long-term oxidation resistance for practical applications of the Al-Co alloys at high temperatures.

4. Conclusions

In the present work, the oxidation behavior of the $Al_{71}Co_{29}$ and $Al_{76}Co_{24}$ alloys (concentration in at.%) was studied at 773–1173 K in air. The alloys were prepared by rapid solidification of Al and Co lumps in argon. The alloys were studied in as-solidified state. The following conclusions can be drawn:

1. The alloys were composed of different microstructure constituents. The $Al_{76}Co_{24}$ alloy was composed of Al_9Co_2, m-$Al_{13}Co_4$ and Z-Al_3Co. The $Al_{71}Co_{29}$ alloy consisted of Z-Al_3Co, Al_5Co_2 and β-AlCo. The precipitation sequences of the constituents were explained based on the equilibrium Al-Co phase diagram and rapid solidification processes taking place during casting.
2. During oxidation in air, aluminum in the alloys was selectively oxidized and a protective alumina scale was formed on the alloy surfaces. The oxidation kinetics followed a parabolic rate law. The rate constants of the alloys were between 1.63×10^{-14} and 8.83×10^{-12} g cm^{-4} s^{-1}, depending on the annealing temperature. The activation energies of oxidation were 90 kJ mol^{-1} for the $Al_{71}Co_{29}$ alloy and 123 kJ mol^{-1} for the $Al_{76}Co_{24}$ alloy, respectively.
3. The scale of the $Al_{76}Co_{24}$ alloy was adherent to the substrate and had a wave-like morphology. At 1173 K, a preferential orientation of θ-Al_2O_3 in (002) crystallographic plane was found. The scale on the $Al_{71}Co_{29}$ alloy was more uniform and spallation was observed locally on the dendritic β-AlCo.
4. The oxidation kinetics of the $Al_{71}Co_{29}$ and $Al_{76}Co_{24}$ alloys was comparable to previously studied $Al_{24}Co_{76}$ and $Al_{32}Co_{68}$ alloys where a continuous alumina scale had been formed. The increased Al concentration contributes to the alloy's corrosion resistance. The continuous Al_2O_3 scale forms a barrier to cobalt diffusion, and it hinders the nucleation and growth of cobalt oxides.

Author Contributions: Conceptualization, M.P., and M.D.; methodology, M.P., M.D., and I.Č.; formal analysis, P.Š.; investigation, P.Š., M.D., I.Č., L.Ď., R.S., Ž.G., and M.P.; resources, M.D., and M.P.; data curation, P.Š., M.P., M.D., I.Č., and L.Ď.; writing—original draft preparation, M.P.; writing—review and editing, M.D., L.Ď., Ž.G., and I.Č.; supervision, M.D., R.S., L.Ď., I.Č., and M.P.; project administration, M.P.; funding acquisition, M.P. All authors have read and agreed to the published version of the manuscript.

Funding: This research was supported by the Grant Agency VEGA of the Slovakian Ministry of Education, Research, Science and Sport project no. 1/0490/18 and by the Slovak Research and Development Agency project no. APVV-15-0049.

Conflicts of Interest: The authors declare no conflict of interest.

References

1. Sato, J.; Omori, T.; Oikawa, K.; Ohnuma, I.; Kainuma, R.; Ishida, K. Cobalt-Base High-Temperature Alloys. *Science* **2006**, *312*, 90–91. [CrossRef]
2. Ma, Q.; Wang, W.; Dong, C. Co-Al-W-based superalloys: A summary of current knowledge. *Cailiao Daobao/ Mater. Rep.* **2020**, *34*, 3157–3164. [CrossRef]
3. Pollock, T.M.; Dibbern, J.; Tsunekane, M.; Zhu, J.; Suzuki, A. New Co-based γ-γ′ high-temperature alloys. *JoM* **2010**, *62*, 58–63. [CrossRef]
4. Betteridge, W.; Shaw, S.W.K. Development of superalloys. *Mater. Sci. Technol.* **1987**, *3*, 682–694. [CrossRef]
5. Coutsouradis, D.; Davin, A.; Lamberigts, M. Cobalt-based superalloys for applications in gas turbines. *Mater. Sci. Eng.* **1987**, *88*, 11–19. [CrossRef]
6. Klarstrom, D.L. Wrought cobalt- base superalloys. *J. Mater. Eng. Perform.* **1993**, *2*, 523–530. [CrossRef]

7. Moffat, J.P.; Whitfield, T.; Christofidou, K.A.; Pickering, E.; Jones, N.; Stone, H.J. The Effect of Heat Treatment on the Oxidation Resistance of Cobalt-Based Superalloys. *Metals* **2020**, *10*, 248. [CrossRef]
8. Liu, L.; Wu, S.-S.; Dong, Y.; Lü, S. Effects of alloyed Mn on oxidation behaviour of a Co-Ni-Cr-Fe alloy between 1050 and 1250 °C. *Corros. Sci.* **2016**, *104*, 236–247. [CrossRef]
9. Holcomb, G.R. Steam Oxidation and Chromia Evaporation in Ultrasupercritical Steam Boilers and Turbines. *J. Electrochem. Soc.* **2009**, *156*, C292–C297. [CrossRef]
10. Forsik, S.A.J.; Rosas, A.O.P.; Wang, T.; Colombo, G.A.; Zhou, N.; Kernion, S.J.; Epler, M.E. High-Temperature Oxidation Behavior of a Novel Co-Base Superalloy. *Met. Mater. Trans. A* **2018**, *49*, 4058–4069. [CrossRef]
11. Klein, L.; Bauer, A.; Neumeier, S.; Göken, M.; Virtanen, S. High temperature oxidation of γ/γ′-strengthened Co-base superalloys. *Corros. Sci.* **2011**, *53*, 2027–2034. [CrossRef]
12. Yan, H.-Y.; Vorontsov, V.; Dye, D. Effect of alloying on the oxidation behaviour of Co-Al-W superalloys. *Corros. Sci.* **2014**, *83*, 382–395. [CrossRef]
13. Goward, G.W.; Cannon, L.W. Pack Cementation Coatings for Superalloys: A Review of History, Theory, and Practice. *J. Eng. Gas Turbines Power* **1988**, *110*, 150–154. [CrossRef]
14. Goward, G. Protective coatings—Purpose, role, and design. *Mater. Sci. Technol.* **1986**, *2*, 194–200. [CrossRef]
15. Goward, G. Progress in coatings for gas turbine airfoils. *Surf. Coat. Technol.* **1998**, *108*, 73–79. [CrossRef]
16. Streiff, R.; Boone, D.H. Corrosion resistant modified aluminide coatings. *J. Mater. Eng.* **1988**, *10*, 15–26. [CrossRef]
17. Meier, G.; Pettit, F. High-temperature corrosion of alumina-forming coatings for superalloys. *Surf. Coat. Technol.* **1989**, *39*, 1–17. [CrossRef]
18. Liu, P.; Liang, K.; Gu, S. High-temperature oxidation behavior of aluminide coatings on a new cobalt-base superalloy in air. *Corros. Sci.* **2001**, *43*, 1217–1226. [CrossRef]
19. Rahman, A.; Jayaganthan, R.; Chandra, R.; Ambardar, R. Microstructural Characterization and Cyclic Hot Corrosion Behaviour of Sputtered Co-Al Nanostructured Coatings on Superalloy. *Oxid. Met.* **2011**, *76*, 307–330. [CrossRef]
20. Rahman, A.; Jayaganthan, R.; Chandra, R.; Ambardar, R. High temperature degradation behavior of sputtered nanostructured Co-Al coatings on superalloy. *Appl. Surf. Sci.* **2013**, *265*, 10–23. [CrossRef]
21. Rahman, A.; Chawla, V.; Jayaganthan, R.; Chandra, R.; Ambardar, R. Degradation behaviour of sputtered Co-Al coatings on superalloy. *Mater. Chem. Phys.* **2013**, *138*, 49–62. [CrossRef]
22. Jiang, J.; Zhou, T.; Shao, W.; Zhou, C. Interdiffusion behavior and lifetime prediction of Co-Al coating on Ni-based superalloy. *J. Alloys Compd.* **2019**, *786*, 920–929. [CrossRef]
23. Stein, F.; He, C.; Dupin, N. Melting behaviour and homogeneity range of B2 CoAl and updated thermodynamic description of the Al-Co system. *Intermetallics* **2013**, *39*, 58–68. [CrossRef]
24. Priputen, P.; Palcut, M.; Babinec, M.; Mišík, J.; Černičková, I.; Janovec, J. Correlation between Microstructure and Corrosion Behavior of Near-Equilibrium Al-Co Alloys in Various Environments. *J. Mater. Eng. Perform.* **2017**, *26*, 3970–3976. [CrossRef]
25. Grushko, B.; Wittenberg, R.; Bickmann, K.; Freiburg, C. The constitution of aluminum-cobalt alloys between Al5Co2 and Al9Co2. *J. Alloys Compd.* **1996**, *233*, 279–287. [CrossRef]
26. Priputen, P.; Kusy, M.; Drienovský, M.; Janičkovič, D.; Čička, R.; Černičková, I.; Janovec, J. Experimental reinvestigation of Al-Co phase diagram in vicinity of Al13Co4 family of phases. *J. Alloys Compd.* **2015**, *647*, 486–497. [CrossRef]
27. Cooper, M.J. The electron distribution in the phases CoAl and NiAl. *Philos. Mag.* **1963**, *8*, 811–821. [CrossRef]
28. Burkhardt, U.; Ellner, M.; Grin, Y.; Baumgartner, B. Powder diffraction refinement of the Co2Al5 structure. *Powder Diffr.* **1998**, *13*, 159–162. [CrossRef]
29. Ma, X.L.; Li, X.Z.; Kuo, K.H. A family of τ-inflated monoclinic Al13Co4 phases. *Acta Crystallogr. Sect. B Struct. Sci.* **1995**, *51*, 36–43. [CrossRef]
30. Freiburg, C.; Grushko, B.; Wittenberg, R.; Reichert, W. Once More about Monoclinic Al13Co4. *Mater. Sci. Forum* **1996**, *228*, 583–586. [CrossRef]
31. Grin, J.; Burkhardt, U.; Ellner, M.; Peters, K. Crystal structure of orthorhombic Co4Al13. *J. Alloys Compd.* **1994**, *206*, 243–247. [CrossRef]
32. Fleischer, F.; Weber, T.; Jung, D.; Steurer, W. o′-Al13Co4, a new quasicrystal approximant. *J. Alloys Compd.* **2010**, *500*, 153–160. [CrossRef]

33. Sugiyama, K.; Genba, M.; Hiraga, K.; Waseda, Y. The structure of Y-Al13-xCo4 (x = 0.8) analyzed by single crystal X-ray diffraction coupled with anomalous X-ray scattering. *J. Alloys Compd.* **2010**, *494*, 98–101. [CrossRef]
34. Boström, M.; Rosner, H.; Prots, Y.; Burkhardt, U.; Grin, Y. The Co2Al9 Structure Type Revisited. *Z. Anorg. Allg. Chem.* **2005**, *631*, 534–541. [CrossRef]
35. Heggen, M.; Deng, D.; Feuerbacher, M. Plastic deformation properties of the orthorhombic complex metallic alloy phase Al13Co4. *Intermetallics* **2007**, *15*, 1425–1431. [CrossRef]
36. Samuel, F.H. A study of the microstructure, mechanical properties and failure behaviour of Al-Li-Co melt-spun ribbons: Effect of Al9Co2 phase particle precipitation. *J. Mater. Sci.* **1986**, *21*, 3097–3107. [CrossRef]
37. Lekatou, A.G.; Sfikas, A.; Karantzalis, A.E. The influence of the fabrication route on the microstructure and surface degradation properties of Al reinforced by Al 9 Co 2. *Mater. Chem. Phys.* **2017**, *200*, 33–49. [CrossRef]
38. Wolf, W.; Schulz, R.; Savoie, S.; Bolfarini, C.; Kiminami, C.S.; Botta, W. Structural, mechanical and thermal characterization of an Al-Co-Fe-Cr alloy for wear and thermal barrier coating applications. *Surf. Coat. Technol.* **2017**, *319*, 241–248. [CrossRef]
39. Hagel, W.C. The oxidation of iron, nickel and cobalt-base alloys containing aluminum. *Corrosion* **1965**, *21*, 316–326. [CrossRef]
40. Young, D.J. Oxidation of Pure Metals. In *High Temperature Oxidation and Corrosion of Metals*, 2nd ed.; Elsevier: Amsterdam, The Netherlands, 2016; Chapter 3; pp. 85–144. [CrossRef]
41. Warde, M.; Herinx, M.; Ledieu, J.; Loli, L.S.; Fournée, V.; Gille, P.; Le Moal, S.; Barthés-Labrousse, M.-G. Adsorption of O2 and C2H (n = 2, 4, 6) on the Al9Co2(0 0 1) and o-Al13Co4(1 0 0) complex metallic alloy surfaces. *Appl. Surf. Sci.* **2015**, *357*, 1666–1675. [CrossRef]
42. Villaseca, S.A.; Loli, L.N.S.; Ledieu, J.; Fournée, V.; Gille, P.; Dubois, J.-M.; Gaudry, É. Oxygen adsorption on the Al9Co2(001) surface: First-principles and STM study. *J. Phys. Condens. Matter* **2013**, *25*, 355003. [CrossRef] [PubMed]
43. Dubois, J.-M. Properties- and applications of quasicrystals and complex metallic alloys. *Chem. Soc. Rev.* **2012**, *41*, 6760. [CrossRef] [PubMed]
44. Wolf, W.; Bolfarini, C.; Kiminami, C.S.; Botta, W. Designing new quasicrystalline compositions in Al-based alloys. *J. Alloys Compd.* **2020**, *823*, 153765. [CrossRef]
45. Steurer, W. Twenty years of structure research on quasicrystals. Part I. Pentagonal, octagonal, decagonal and dodecagonal quasicrystals. *Z. Krist. Cryst. Mater.* **2004**, *219*, 391–446. [CrossRef]
46. Barber, E.M. Chemical Bonding and Physical Properties in Quasicrystals and Their Related Approximant Phases: Known Facts and Current Perspectives. *Appl. Sci.* **2019**, *9*, 2132. [CrossRef]
47. Rabson, D. Toward theories of friction and adhesion on quasicrystals. *Prog. Surf. Sci.* **2012**, *87*, 253–271. [CrossRef]
48. Balbyshev, V.; King, D.; Khramov, A.; Kasten, L.; Donley, M. Investigation of quaternary Al-based quasicrystal thin films for corrosion protection. *Thin Solid Films* **2004**, *447*, 558–563. [CrossRef]
49. Moskalewicz, T.; Dubiel, B.; Wendler, B. AlCuFe(Cr) and AlCoFeCr coatings for improvement of elevated temperature oxidation resistance of a near-α titanium alloy. *Mater. Charact.* **2013**, *83*, 161–169. [CrossRef]
50. Parsamehr, H.; Chang, S.-Y.; Lai, C.-H. Mechanical and surface properties of aluminum-copper-iron quasicrystal thin films. *J. Alloy Compd.* **2018**, *732*, 952–957. [CrossRef]
51. Parsamehr, H.; Chen, T.-S.; Wang, D.-S.; Leu, M.-S.; Han, I.; Xi, Z.; Tsai, A.-P.; Shahani, A.J.; Lai, C.-H. Thermal spray coating of Al-Cu-Fe quasicrystals: Dynamic observations and surface properties. *Materialia* **2019**, *8*, 100432. [CrossRef]
52. Chatelier, C.; Garreau, Y.; Piccolo, L.; Vlad, A.; Resta, A.; Ledieu, J.; Fournée, V.; De Weerd, M.-C.; Picca, F.-E.; De Boissieu, M.; et al. From the Surface Structure to Catalytic Properties of Al5Co2($2\bar{1}0$): A Study Combining Experimental and Theoretical Approaches. *J. Phys. Chem. C* **2020**, *124*, 4552–4562. [CrossRef]
53. Piccolo, L.; Chatelier, C.; De Weerd, M.-C.; Morfin, F.; Ledieu, J.; Fournée, V.; Gille, P.; Gaudry, E. Catalytic properties of Al13TM4 complex intermetallics: Influence of the transition metal and the surface orientation on butadiene hydrogenation. *Sci. Technol. Adv. Mater.* **2019**, *20*, 557–567. [CrossRef] [PubMed]
54. Meier, M.; Ledieu, J.; Fournée, V.; Gaudry, E. Semihydrogenation of Acetylene on Al5Co2 Surfaces. *J. Phys. Chem. C* **2017**, *121*, 4958–4969. [CrossRef]
55. Soler, L.; Macanás, J.; Muñoz, M.; Casado, J. Aluminum and aluminum alloys as sources of hydrogen for fuel cell applications. *J. Power Sources* **2007**, *169*, 144–149. [CrossRef]

56. Lekatou, A.G.; Sfikas, A.; Karantzalis, A.E.; Sioulas, D. Microstructure and corrosion performance of Al-32%Co alloys. *Corros. Sci.* **2012**, *63*, 193–209. [CrossRef]
57. Palcut, M.; Priputen, P.; Kusý, M.; Janovec, J. Corrosion behaviour of Al-29at%Co alloy in aqueous NaCl. *Corros. Sci.* **2013**, *75*, 461–466. [CrossRef]
58. Palcut, M.; Priputen, P.; Šalgó, K.; Janovec, J. Phase constitution and corrosion resistance of Al-Co alloys. *Mater. Chem. Phys.* **2015**, *166*, 95–104. [CrossRef]
59. Zhang, H.H.; Xiang, J.; Wang, W.; Shi, Y.-J. The Oxidation of Co-5Al Alloys in 1 Atm of Pure O2 at 700 and 800 °C. *Adv. Mater. Res.* **2011**, *295*, 319–322. [CrossRef]
60. Zhang, H.H.; Xiang, J.H.; Xu, X.C.; Wang, C. Comparison of Oxidation Behavior of Binary Co-10X (x = Al, Si, Cr) Alloys at 973 and 1073K. *Appl. Mech. Mater.* **2013**, *395*, 238–242. [CrossRef]
61. Irving, G.N.; Stringer, J.; Whittle, D.P. The high-temperature oxidation resistance of Co-Al alloys. *Oxid. Met.* **1975**, *9*, 427–440. [CrossRef]
62. Agliozzo, S.; Brunello, E.; Klein, H.; Mancini, L.; Hartwig, J.; Baruchel, J.; Gastaldi, J. Extended investigation of porosity in quasicrystals by synchrotron X-ray phase contrast radiography—I: In icosahedral AlPdMn grains. *J. Cryst. Growth* **2005**, *281*, 623–638. [CrossRef]
63. Brunello, E.; Agliozzo, S.; Klein, H.; Mancini, L.; Härtwig, J.; Baruchel, J.; Gastaldi, J. Extended investigation of porosity in quasicrystals by synchrotron X-ray phase contrast radiography: Part II, in grains of other alloys and structures than AlPdMn. *J. Cryst. Growth* **2005**, *282*, 228–235. [CrossRef]
64. Prescott, R.; Graham, M.J. The oxidation of iron-aluminum alloys. *Oxid. Met.* **1992**, *38*, 73–87. [CrossRef]
65. Chevalier, S. Formation and growth of protective alumina scales. In *Developments in High Temperature Corrosion and Protection of Materials*, 1st ed.; Woodhead Publishing: Abington, Cambridge, UK, 2008; Chapter 10; pp. 290–328. [CrossRef]
66. Wehner, B.I.; Köster, U. Microstructural Evolution of Alumina Layers on an Al-Cu-Fe Quasicrystal during High-Temperature Oxidation. *Oxid. Met.* **2000**, *54*, 445–456. [CrossRef]
67. Tolpygo, V.; Clarke, D.R. Microstructural evidence for counter-diffusion of aluminum and oxygen during the growth of alumina scales. *Mater. High Temp.* **2003**, *20*, 261–271. [CrossRef]
68. Dan'Ko, A.J.; Rom, M.A.; Sidelnikova, N.S.; Nizhankovskiy, S.V.; Budnikov, A.T.; Grin', L.A.; Kaltaev, K.S.-O. Transformation of the corundum structure upon high-temperature reduction. *Crystallogr. Rep.* **2008**, *53*, 1112–1118. [CrossRef]
69. Trunov, M.A.; Schoenitz, M.; Zhu, X.; Dreizin, E.L. Effect of polymorphic phase transformations in Al2O3 film on oxidation kinetics of aluminum powders. *Combust. Flame* **2005**, *140*, 310–318. [CrossRef]
70. Zhou, R.S.; Snyder, R.L. Structures and transformation mechanisms of the η, γ and θ transition aluminas. *Acta Crystallogr. Sect. B Struct. Sci.* **1991**, *47*, 617–630. [CrossRef]
71. Kovarik, L.; Bowden, M.; Shi, D.; Washton, N.M.; Andersen, A.; Hu, J.Z.; Lee, J.; Szanyi, J.; Kwak, J.-H.; Peden, C.H.F. Unraveling the Origin of Structural Disorder in High Temperature Transition Al2O3: Structure of θ-Al2O3. *Chem. Mater.* **2015**, *27*, 7042–7049. [CrossRef]
72. Jbara, A.S.; Othaman, Z.; Saeed, M. Structural, morphological and optical investigations of θ-Al2O3 ultrafine powder. *J. Alloys Compd.* **2017**, *718*, 1–6. [CrossRef]
73. Wang, Y.; Bronsveld, P.; De Hosson, J.T.M.; Djuričić, B.; McGarry, D.; Pickering, S. Twinning in θ Alumina Investigated with High Resolution Transmission Electron Microscopy. *J. Eur. Ceram. Soc.* **1998**, *18*, 299–304. [CrossRef]
74. Kovarik, L.; Bowden, M.; Andersen, A.; Jaegers, N.R.; Washton, N.; Szanyi, J. Quantification of High Temperature Transitions and Their Phase Transformations. Available online: https://chemrxiv.org/articles/preprint/Quantification_of_High_Temperature_Transition_Al2O3_and_Their_Phase_Transformations/12584783 (accessed on 4 July 2020).
75. Boumaza, A.; Favaro, L.; Ledion, J.; Sattonnay, G.; Brubach, J.; Berthet, P.; Huntz, A.; Roy, P.; Tétot, R. Transition alumina phases induced by heat treatment of boehmite: An X-ray diffraction and infrared spectroscopy study. *J. Solid State Chem.* **2009**, *182*, 1171–1176. [CrossRef]
76. McCafferty, E. High-Temperature Gaseous Oxidation. In *Introduction to Corrosion Science*; Springer: New York, NY, USA, 2009; pp. 453–476. [CrossRef]
77. Ledieu, J.; Gaudry, E.; Fournée, V. Surfaces of Al-based complex metallic alloys: Atomic structure, thin film growth and reactivity. *Sci. Technol. Adv. Mater.* **2014**, *15*, 34802. [CrossRef] [PubMed]

78. Korte-Kerzel, S.; Schnabel, V.; Clegg, W.; Heggen, M. Room temperature plasticity in m-Al13Co4 studied by microcompression and high resolution scanning transmission electron microscopy. *Scr. Mater.* **2018**, *146*, 327–330. [CrossRef]
79. Wang, W.; Yang, W.; Liu, Z.; Lin, Y.; Zhou, S.; Qian, H.; Wang, H.; Lin, Z.; Li, G. Epitaxial growth and characterization of high-quality aluminum films on sapphire substrates by molecular beam epitaxy. *CrystEngComm* **2014**, *16*, 7626–7632. [CrossRef]
80. Alessandri, M.; Piagge, R.; Caniatti, M.; Del Vitto, A.; Wiemer, C.; Pavia, G.; Alberici, S.; Bellandi, E.; Nale, A. Structural and Chemical Investigation of Annealed Al2O3 Films for Interpoly Dielectric Application in Flash Memories. *ECS Trans.* **2006**, *3*, 183–192. [CrossRef]
81. Queraltó, A.; De La Mata, M.; Arbiol, J.; Obradors, X.; Puig, T. Disentangling Epitaxial Growth Mechanisms of Solution Derived Functional Oxide Thin Films. *Adv. Mater. Interfaces* **2016**, *3*, 1600392. [CrossRef]
82. Mattox, D.M. Atomistic Film Growth and Some Growth-Related Film Properties. In *Handbook of Physical Vapor Deposition (PVD) Processing*, 2nd ed.; Elsevier: Oxford, UK, 2010; pp. 333–398. [CrossRef]
83. Meier, M.; Ledieu, J.; De Weerd, M.-C.; Huang, Y.-T.; Abreu, G.J.P.; Pussi, K.; Diehl, R.; Mazet, T.; Fournée, V.; Gaudry, E. Interplay between bulk atomic clusters and surface structure in complex intermetallic compounds: The case study of the Al5Co2(001) surface. *Phys. Rev. B* **2015**, *91*, 085414. [CrossRef]
84. Anand, K.; Fournée, V.; Prevot, G.; Ledieu, J.; Gaudry, E. Nonwetting Behavior of Al-Co Quasicrystalline Approximants Owing to Their Unique Electronic Structures. *ACS Appl. Mater. Interfaces* **2020**, *12*, 15793–15801. [CrossRef]
85. Gulbransen, E.A.; Wysong, W.S. Thin Oxide Films on Aluminum. *J. Phys. Chem.* **1947**, *51*, 1087–1103. [CrossRef]
86. Smeltzer W, W. Oxidation of An Aluminum-3 Per Cent Magnesium Alloy in the Temperature Range 200–550 °C. *J. Electrochem. Soc.* **1958**, *105*, 67–71. [CrossRef]
87. Sabat, K.C.; Paramguru, R.K.; Pradhan, S.; Mishra, B.K. Reduction of Cobalt Oxide (Co3O4) by Low Temperature Hydrogen Plasma. *Plasma Chem. Plasma Process.* **2014**, *35*, 387–399. [CrossRef]
88. Chattopadhyay, B.; Wood, G.C. The transient oxidation of alloys. *Oxid. Met.* **1970**, *2*, 373–399. [CrossRef]
89. Stott, F.H. Influence of alloy additions on oxidation. *Mater. Sci. Technol.* **1989**, *5*, 734–740. [CrossRef]
90. Wehner, B.; Köster, U.; Rüdiger, A.; Pieper, C.; Sordelet, D. Oxidation of Al–Cu–Fe and Al–Pd–Mn quasicrystals. *Mater. Sci. Eng. A* **2000**, *294*, 830–833. [CrossRef]
91. Prud'Homme, N.; Ribot, P.; Herinx, M.; Gille, P.; Bauer, B.; De Weerd, M.-C.; Barthés-Labrousse, M.-G. High temperature oxidation of AlCrFe complex metallic alloys. *Corros. Sci.* **2014**, *89*, 118–126. [CrossRef]
92. Irving, G.N.; Stringer, J.; Whittle, D.P. The Oxidation Behavior of Co-Cr-Al Alloys at 1000 °C. *Corrosion* **1977**, *33*, 56–60. [CrossRef]
93. Wood, G.C.; Stott, F.H. The influence of aluminum additions on the oxidation of Co-Cr alloys at 1000 and 1200 °C. *Oxid. Met.* **1971**, *3*, 365–398. [CrossRef]